

Hot deformation behavior, processing map, and microstructural evolution of Mg-Zn-Zr magnesium alloy

Yingbao Li¹, Ran Li¹, Guojun Cai¹, R. D. K. Misra²

¹School of Mechanical Engineering, Liaoning Petrochemical University, Fushun 113001, P. R. China

²Laboratory for Excellence in Advanced Steel Research, Department of Metallurgical, Materials and Biomedical Engineering, University of Texas at El Paso, El Paso, TX 79968, USA

Received 30 March 2023, received in revised form 18 April 2023, accepted 1 June 2023

Abstract

The hot compression in the deformation temperature range of 523–673 K and strain rates of 0.001–1 s⁻¹ was aimed to study the hot deformation behavior, processing map, and dynamic recrystallization (DRX) to confirm an optimum hot working condition of Mg-Zn-Zr alloy. The strain-stress results by using the Gleeble-1500 simulator indicated that the flow stress decreases with increasing temperature or decreasing of strain rates, and the Medium Gaussian Kernel (correlation coefficient (R) = 0.9806, absolute relative error (AARE) = 3.28 %) has better predicting capacity. Based on the processing map and constitutive equation, the optimum hot-working condition for Mg alloys can be determined to be at hot compression temperature and strain rates in the range of 593–623 K and 0.01–0.001 s⁻¹ with a peak value of power dissipation efficiency (PDE) which is reaching to 37 %.

Key words: Mg-Zn-Zr, hot deformation, processing map, dynamic recrystallization

1. Introduction

Magnesium (Mg) and its alloys have attracted plenty of attention in the automotive and aerospace industries, and become a promising candidate to replace traditional alloy steels due to their high specific strength and lightweight [1–4]. So far, the development of wrought Mg alloys is still subject to many restrictions because of the lower ductility and plastic deformation capacity at room temperature [5–9]. On the one hand, owing to the low symmetry of the hcp structure, few independent slip systems can be activated at room temperature, resulting in poor room temperature plasticity of wrought magnesium alloy [10–14]. On the other hand, Mg alloys prepared by rolling or extrusion often form strong basal texture, causing an obvious anisotropy and high tension and compression asymmetry [15–18].

Based on the poor cell symmetry of Mg alloys, only the (0002) $\langle 11\bar{2}0 \rangle$ slip system has lower critical shear stress and is easy to be activated, rather than other slip systems such as prismatic slip $\langle a \rangle$ slip ($\{10\bar{1}0\} \langle 11\bar{2}0 \rangle$), pyramidal $\langle a \rangle$ slip ($\{10\bar{1}1\} \langle 11\bar{2}0 \rangle$),

and pyramidal $\langle c + a \rangle$ slip ($\{11\bar{2}2\} \langle 11\bar{2}3 \rangle$), as the critical shear stress is very high, which results in poor bending ability of magnesium alloys at room temperature, and they cannot be bent to a large extent or even flanged like Al alloys [19–22]. Therefore, it is necessary to initiate non-basal slip for Mg alloys during the plastic deformation.

In this study, the present work has been focused on the dynamic recrystallization softening behavior based on the flow stress curves (deformation temperature ranging from 523 to 673 K), and the change in texture and microstructural evolution.

2. Experimental procedure

2.1. Sample preparation

The raw materials (pure 99.99 % Mg, 99.95 % Zn, and 99.92 % Zr, etc.) were melted in a electric furnace equipped a protection atmosphere of N₂ with a high mandatory infiltration stirring rate (7000 rmp) for 3–5 min at 973 K, and then this melt was molded in ø

*Corresponding author: e-mail address: cglj197800@163.com

Table 1. Chemical composition of Mg alloy (wt.%)

| Alloy | Zn | Zr | Mn | Al | Fe | Si | Mg |
|----------|-----|------|------|------|-------|-------|------|
| Mg-Zn-Zr | 5.8 | 0.42 | 0.06 | 0.03 | 0.014 | 0.005 | bal. |

140 mm × 180 mm metal pattern to get an ingot, the chemical composition of Mg-Zn-Zr alloy was summarized in Table 1.

The cast ingots were machined into cylindrical specimens with ϕ 10 mm × 10 mm dimension for hot compression tests carried out using an MMS-300 servo hydraulic thermomechanical simulator. The thermo-mechanical processing schedule of specimens under different conditions is shown in Fig. 1. These specimens suffered a hot compression using a Gleeble-1500 thermal simulation test machine at four temperatures (523, 573, 623, and 673 K), and different strain rates (0.001, 0.01, 0.1, and 1 s^{-1}), and then they were quenched in water to obtain their microstructures.

Microstructures taken from the center of the transversal section after isothermal hot compression were observed by scanning electron microscopy (SEM) equipped with electron backscattered diffrac-

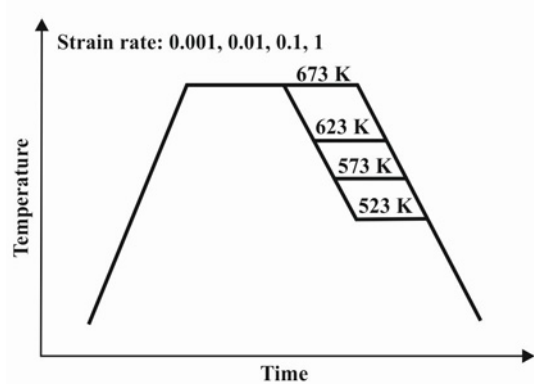
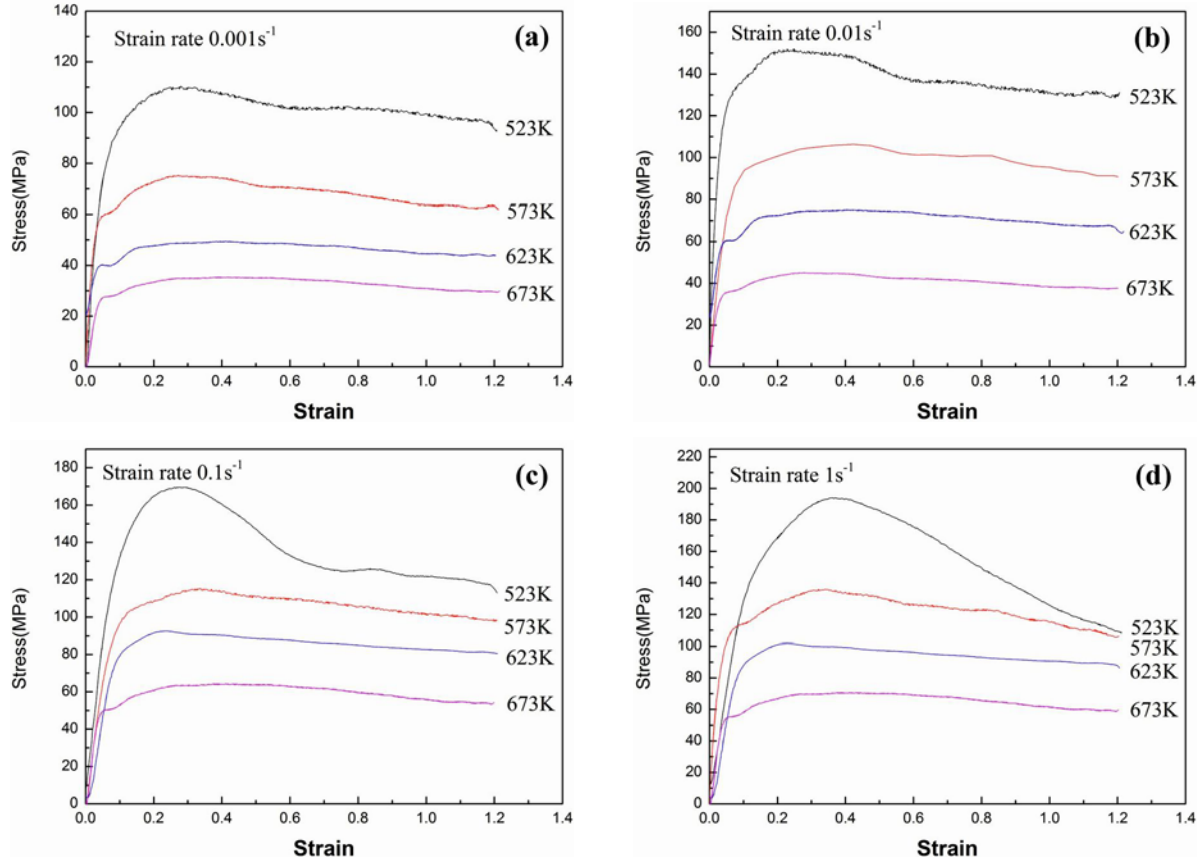


Fig. 1. Thermomechanical processing schedule.

tion (EBSD) after etching with a mixture solution of 1 g oxalic acid + 1 mL acetic acid + 1 mL nitric acid + 100 mL water.

After using a three-axis ion beam polishing technique, the data analysis of samples was studied by *EDAX-TSL 7.0 software* to investigate the grain boundary character distribution (GBCD), textures and inverse pore figure (IPF) diagram on compression axis.

Fig. 2. Compressive stress-strain curves for samples at a strain rate of (a) 0.001 s^{-1} , (b) 0.01 s^{-1} , (c) 0.1 s^{-1} , and (d) 1 s^{-1} .

3. Results and discussion

3.1. Stress-strain behavior

Figure 2 presents the compressive stress-strain curves of specimens obtained under various compression conditions. Apparently, the flow stress increases rapidly with a stationary work-hardening rate during their initial stage of compression deformation. After that, the stress rises to a peak value with an increase in strain, and the work-hardening rate witnesses a downward trend, manifesting the occurrence of a dynamic softening process. Then the flow stress decreases slowly with the strain because the dynamic softening effect transcends the work-hardening effect, while a final steady state means a result of balance between them.

Based on the constitutive equation, a relationship between some deformation parameters (deformation temperature and strain rate) and flow stress of Mg alloys provides a simulation basis for the final determination of deformation parameters in industrial production. The microstructure evolution during thermally activated deformation is dependent on thermal deformation temperature (T), stress, strain (ε), and strain rate ($\dot{\varepsilon}$). The relationship between the activation energy (Q) and deformation parameters can be determined by Zener-Hollomon parameter (Z) [23]:

$$Z = \dot{\varepsilon} \exp\left(\frac{Q}{RT}\right) = A [\sinh(\alpha\sigma)]^n. \quad (1)$$

Based on a relevant relation of thermal deformation in a typical hyperbolic-sine form, $\dot{\varepsilon}$ is calculated by:

$$\dot{\varepsilon} = A [\sinh(\alpha\sigma)]^n \exp\left(-\frac{Q}{RT}\right), \quad (2)$$

$$\dot{\varepsilon} = A_1 \sigma^n \exp\left(-\frac{Q}{RT}\right), \quad (\text{low stress level}) \quad (3)$$

$$\dot{\varepsilon} = A_2 \exp(\beta\sigma) \exp\left(-\frac{Q}{RT}\right), \quad (\text{high stress level}) \quad (4)$$

where A , A_1 , A_2 , β , α , and R (8.314 J K^{-1}) are some corresponding material constants, while σ and T represent the peak flow stress (MPa) and absolute temperature (K), and n shows stress exponent. α , n , and Q can be calculated under various deformation temperatures and strain rates to indicate the difficulty of plastic deformation of alloys. Taking natural logarithm on the above equation [24], they can be written as:

$$\ln \dot{\varepsilon} = \ln A_1 + n \ln \sigma - \frac{Q}{RT}, \quad (5)$$

$$\ln \dot{\varepsilon} = \ln A_2 + \beta \sigma - \frac{Q}{RT}. \quad (6)$$

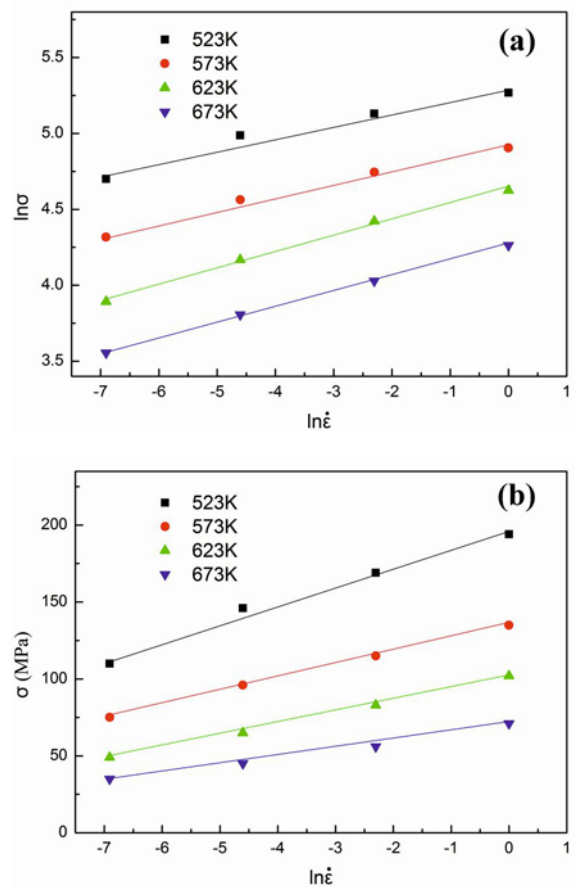


Fig. 3. Relationship between flow stress and strain rate for samples: (a) $\ln \dot{\varepsilon} - \ln \sigma$ and (b) $\ln \dot{\varepsilon} - \sigma$.

After given compression temperature, Eq. (2) can be combined by taking the natural logarithm:

$$\ln \dot{\varepsilon} = \ln A + n \ln [\sinh(\alpha\sigma)] - \frac{Q}{RT}, \quad (\text{any stress level}). \quad (7)$$

Based on Eq. (7), Q is obtained at a given strain rate as follows:

$$\partial(\ln \dot{\varepsilon}) = \partial n \{\ln [\sinh(\alpha\sigma)]\} - \frac{Q}{RT} \partial\left(\frac{1}{T}\right), \quad (8)$$

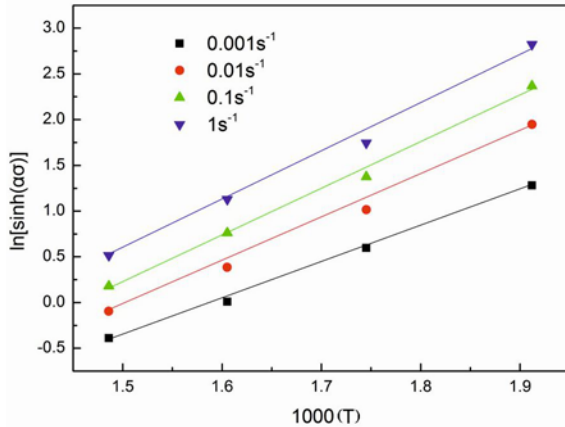
$$n = \left[\frac{\partial(\ln \dot{\varepsilon})}{\partial \{\ln [\sinh(\alpha\sigma)]\}} \right]_T, \quad (9)$$

$$Q = nR \left[\frac{\partial \{\ln [\sinh(\alpha\sigma)]\}}{\partial(1/T)} \right]_{\dot{\varepsilon}} = nRS. \quad (10)$$

A relationship between flow stress and strain rate for alloys under various combinations is shown in Fig. 3. As expected, the peak stress of alloys is vulnerable to strain rate, and it decreases with increasing of deformation temperature. The linear regression is obtained using the least square method, and their n

Table 2. Coefficients of polynomial for α , n , Q , and $\ln A$ of samples

| α | n | Q (kJ mol $^{-1}$) | $\ln A$ |
|------------------|------------------|-----------------------|------------------|
| $a_0 = 0.02382$ | $b_0 = 7.275$ | $c_0 = 216.022$ | $d_0 = 36.183$ |
| $a_1 = -0.04264$ | $b_1 = -25.481$ | $c_1 = -209.693$ | $d_1 = -31.782$ |
| $a_2 = 0.18218$ | $b_2 = 82.284$ | $c_2 = 319.557$ | $d_2 = 33.569$ |
| $a_3 = -0.29405$ | $b_3 = -111.709$ | $c_3 = -951.566$ | $d_3 = -104.846$ |
| $a_4 = 0.13573$ | $b_4 = 44.167$ | $c_4 = 1752.308$ | $d_4 = 191.459$ |
| $a_5 = 0.01619$ | $b_5 = 18.908$ | $c_5 = -907.745$ | $d_5 = -107.404$ |

Fig. 4. Relationship between $\ln [\sinh (\alpha\sigma)]$ and $1000/T$ for samples.

values at different temperatures can be calculated depending on the average slope value of straight lines provided in Fig. 3a, and the average n value is dependent on the average slope value of straight lines in Fig. 3b, and Eq. (7) is expressed by:

$$\ln [\sinh (\alpha\sigma)] = \frac{Q}{1000 \cdot nR} \frac{1000}{T} + \frac{\ln \dot{\varepsilon} - \ln A}{n}. \quad (11)$$

Likewise, the least square calculation method is used for the slope of the linear regression lines to account for the relevant curves between $\ln [\sinh(\alpha\sigma)]$ and $1000/T$ for alloys, as provided in Fig. 4. Then the activation energy of samples is obtained by given value of $Q/1000nR$.

In order to reduce calculation errors, the constitutive models are modified to calculate the material constants of alloys (Q , n , $\ln A$, and α) at various strains due to complex relationship between these constants and strains, and they are obtained by a 5th-order polynomial, written as:

$$\left\{ \begin{array}{l} \alpha = a_0 + a_1\varepsilon + a_2\varepsilon^2 + a_3\varepsilon^3 + a_4\varepsilon^4 + a_5\varepsilon^5 \\ n = b_0 + b_1\varepsilon + b_2\varepsilon^2 + b_3\varepsilon^3 + b_4\varepsilon^4 + b_5\varepsilon^5 \\ Q = c_0 + c_1\varepsilon + c_2\varepsilon^2 + c_3\varepsilon^3 + c_4\varepsilon^4 + c_5\varepsilon^5 \\ \ln A = d_0 + d_1\varepsilon + d_2\varepsilon^2 + d_3\varepsilon^3 + d_4\varepsilon^4 + d_5\varepsilon^5 \end{array} \right. \quad (12)$$

Considering a different compensation of strains, these modified constitutive equations can effectively predict flow stress at various strains. Based on Table 2, the coefficients of polynomial for material constants of sample can be given as follows:

$$\left\{ \begin{array}{l} \alpha = 0.02382 - 0.04264\varepsilon + 0.18218\varepsilon^2 \\ \quad - 0.29405\varepsilon^3 + 0.13573\varepsilon^4 + 0.01619\varepsilon^5 \\ n = 7.275 - 25.481\varepsilon + 82.284\varepsilon^2 - 111.709\varepsilon^3 \\ \quad + 44.167\varepsilon^4 + 18.908\varepsilon^5 \\ Q = 216.022 - 209.693\varepsilon + 319.557\varepsilon^2 \\ \quad - 951.566\varepsilon^3 + 1752.308\varepsilon^4 - 907.745\varepsilon^5 \\ \ln A = 36.183 - 31.782\varepsilon + 33.569\varepsilon^2 \\ \quad - 104.846\varepsilon^3 + 191.459\varepsilon^4 - 107.404\varepsilon^5 \end{array} \right. \quad (13)$$

To further predict flow stress, the relationship between the average absolute relative error (AARE) and correlation coefficient (R) is expressed by:

$$R = \frac{\sum_{i=1}^N (E_i - \bar{E})(C_i - \bar{C})}{\sqrt{\sum_{i=1}^N (E_i - \bar{E})^2 \sum_{i=1}^N (C_i - \bar{C})^2}}, \quad (14)$$

$$\text{AARE} (\%) = \frac{1}{N} \sum_{i=1}^N \left| \frac{E_i - C_i}{E_i} \right| \times 100, \quad (15)$$

where E is the obtained experimental data, while N is the number of experimental data, and C is the predicted value be written in the modified constitutive equation, in this case, \bar{E} and \bar{C} are defined as the values of E and C , respectively. R can be utilized to calculate the linearity between calculated and experimental data, and AARE means the average-relative errors, which precisely assesses the calculated data.

After calculated, R and AARE values of alloys are found to be 99.025 % and 3.28 %, verifying the accuracy and reliability of modified constitutive equations under deformation conditions for alloys. The decreasing of peak stress by recrystallization softening effect causes a decrease in activation energy, and the lower Q value of materials means the more the dynamic recrystallization.

Figure 5 reveals the processing maps of alloys at strains of 0.4 and 1.2, and the peak efficiency of power

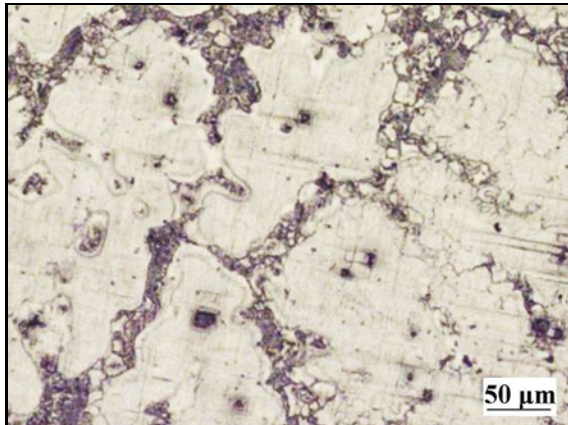


Fig. 5. Processing maps of samples at strains of: (a) 0.4 and (b) 1.2, with peak efficiency of power dissipation domains being indicated by colored rectangles and the instability domains by shaded areas.

dissipation domains can be indicated by blue rectangles while the instability domains is represented by

some shaded areas. Compared with the corresponding blue rectangles draw at strain of 0.4, all of those draw at strain of 1.2 extend to a relatively lower deformation temperature range, revealing that the workability of alloys can be effectively enhanced with the corresponding progress of compression. It is believed that an instability occurs at higher strain rates ($> 1 \text{ s}^{-1}$) and lower temperature range ($< 673 \text{ K}$) at strain of 0.4, while an invasion of instability domain to a relatively higher temperature ($> 673 \text{ K}$) can be observed when a strain increases to 1.2.

The strain rate and temperature failing in region of the higher η can be identified as an optimum working area, and the peak value of power dissipation efficiency which is to reach to 31 %. Meanwhile, the working parameters for avoiding flow instability can be obtained according to red regions of processing map.

3.2. Microstructure

Figure 6 presents the microstructures, GBCD and inverse pole figures of specimens at different de-

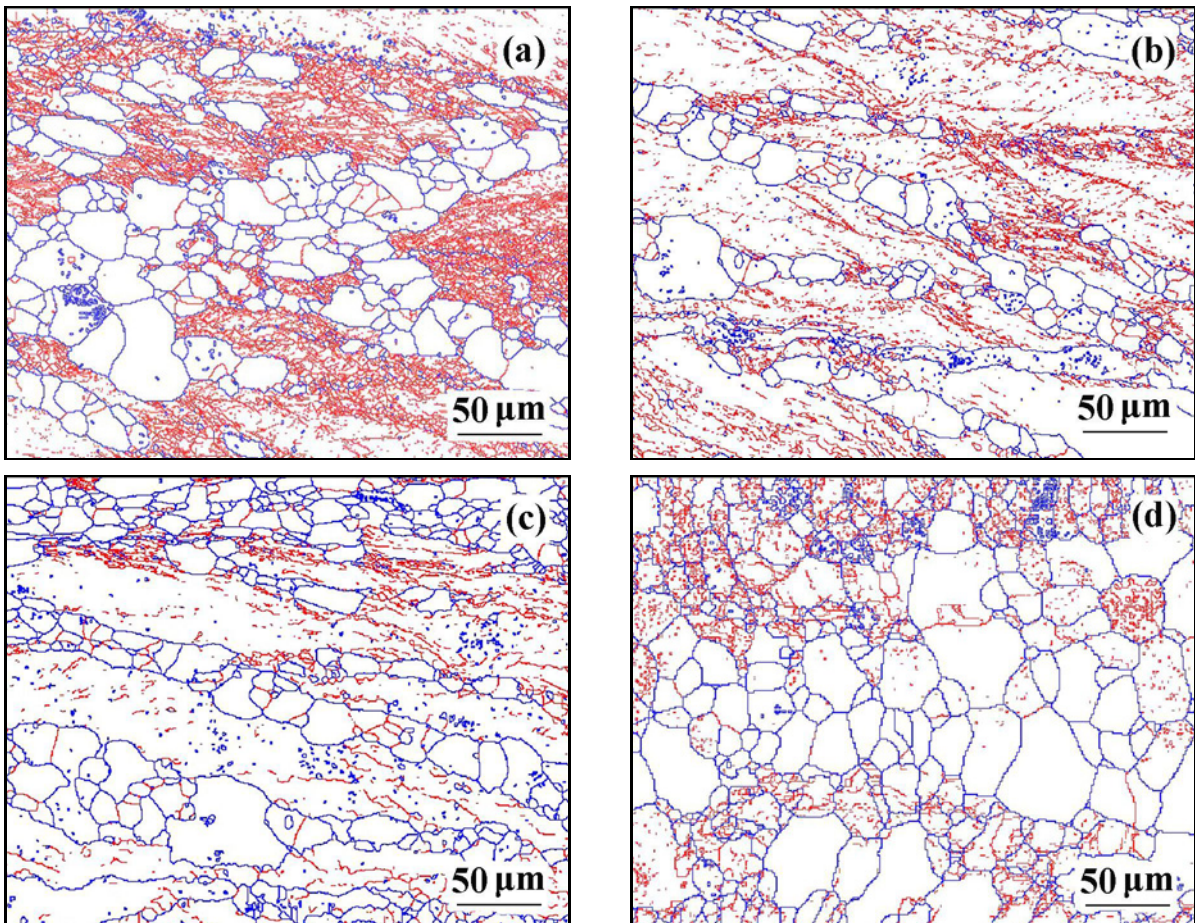


Fig. 6. Microstructures, grain boundary types and inverse pole figures of specimens deformed at (a) 523 K & 0.1 s^{-1} , (b) 573 K & 0.1 s^{-1} , (c) 623 K & 0.1 s^{-1} , and (d) 673 K & 0.1 s^{-1} (red and blue represent LAGBs (5° – 15°) and HAGBs (15° – 180°), respectively).

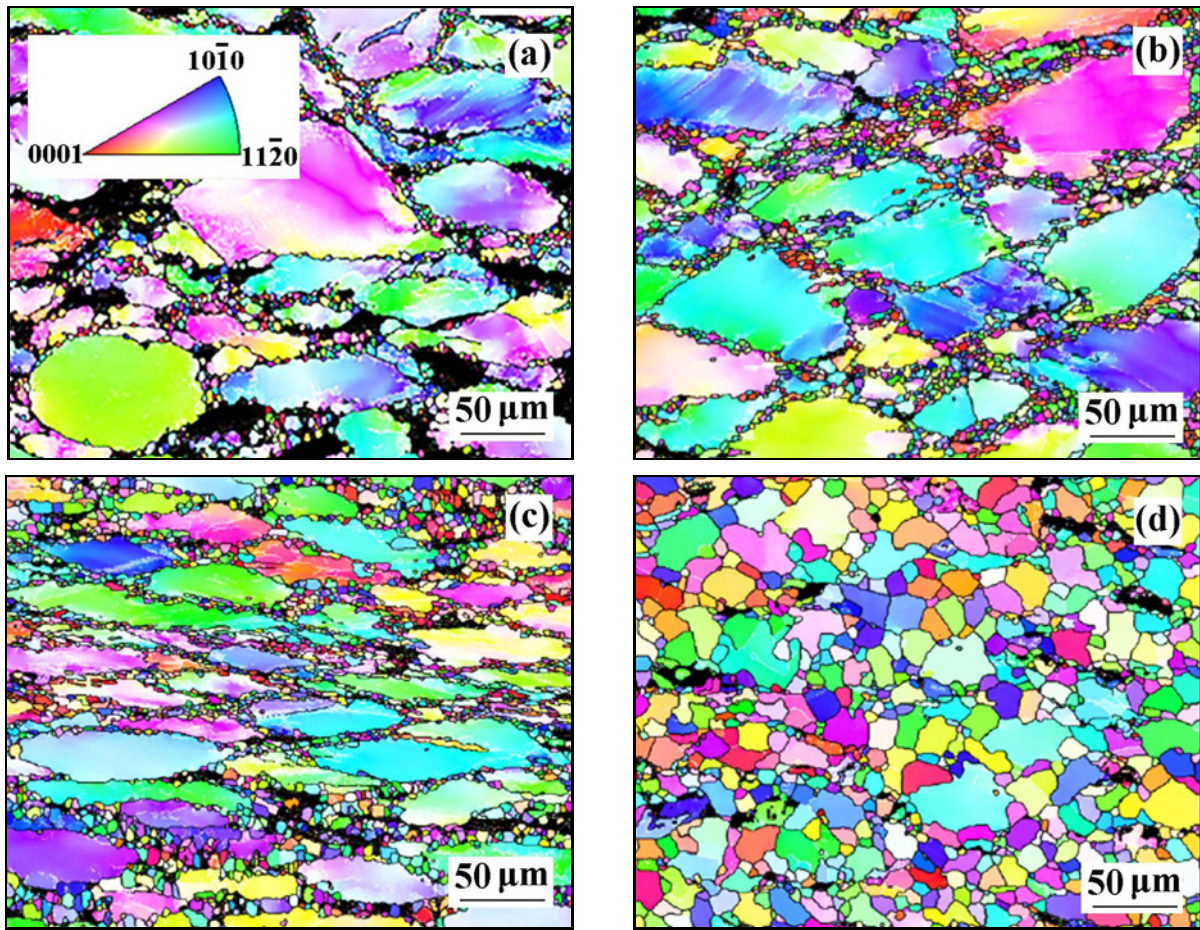


Fig. 7. IPF diagram of specimens deformed at (a) 523 K & 0.001 s^{-1} , (b) 573 K & 0.001 s^{-1} , (c) 623 K & 0.001 s^{-1} , and (d) 673 K & 0.001 s^{-1} .

formation temperatures. The specimen deformed at 523 K & 0.1 s^{-1} is characterized by a large number of sub-structures with the low angle grain boundaries (LAGBs), which have been encircled by several typical necklace structures, as shown in Fig. 6a. Generally, the initial grain boundaries are places where the higher density dislocations are easier to accumulate and thus are favorable sites for the formation of some sub-structures. With temperature increasing, these sub-structures walled by LAGBs gradually decrease, while the recrystallized grains presenting a considerable increment as the number of high angle grain boundaries (HAGBs) increase (Fig. 6d).

Figure 7 reveals the simulation of recrystallization at strain rate 0.001 s^{-1} under different deformation temperatures. As can be seen from the figures, at the same strain rate, the dynamic recrystallization volume fraction increases with the increase of temperature, and the grain shape gradually changes from flat to equiaxed. The dynamic recrystallization grains at 523 and 573 K are finer than those at 623 and 673 K. Although the increase of temperature shortens the incubation period of nucleation and forms more small nuclei, it can make the atomic transition

at the grain boundary become more frequent. Then the speed of grain boundary migration can be accelerated, which makes the grains grow faster and become coarser. It is well-known that at higher temperature, the critical strain of dynamic recrystallization is smaller, and the completion of dynamic recrystallization is earlier [25]. However, because higher temperature is conducive to grain growth, the average grain size in the stable state is also larger, and the critical dislocation density required for dynamic recrystallization is reduced with increasing temperature [26]. Therefore, when the temperature is 400°C (673 K) and the strain rate is 0.001 s^{-1} , the dynamic recrystallization volume fraction is the largest, and the grain shape is closer to that of equiaxed grain, and the distribution of microstructures is more uniform.

Figure 8 shows the pole figures of specimens deformed at strain rate 0.001 s^{-1} under different deformation temperatures. Almost all these samples have the basal texture type, and the intensity decreases with the increase in temperature. It can be seen from Fig. 8a that the plate presents a typical basal texture, which is not strong, and the weakly oriented compo-

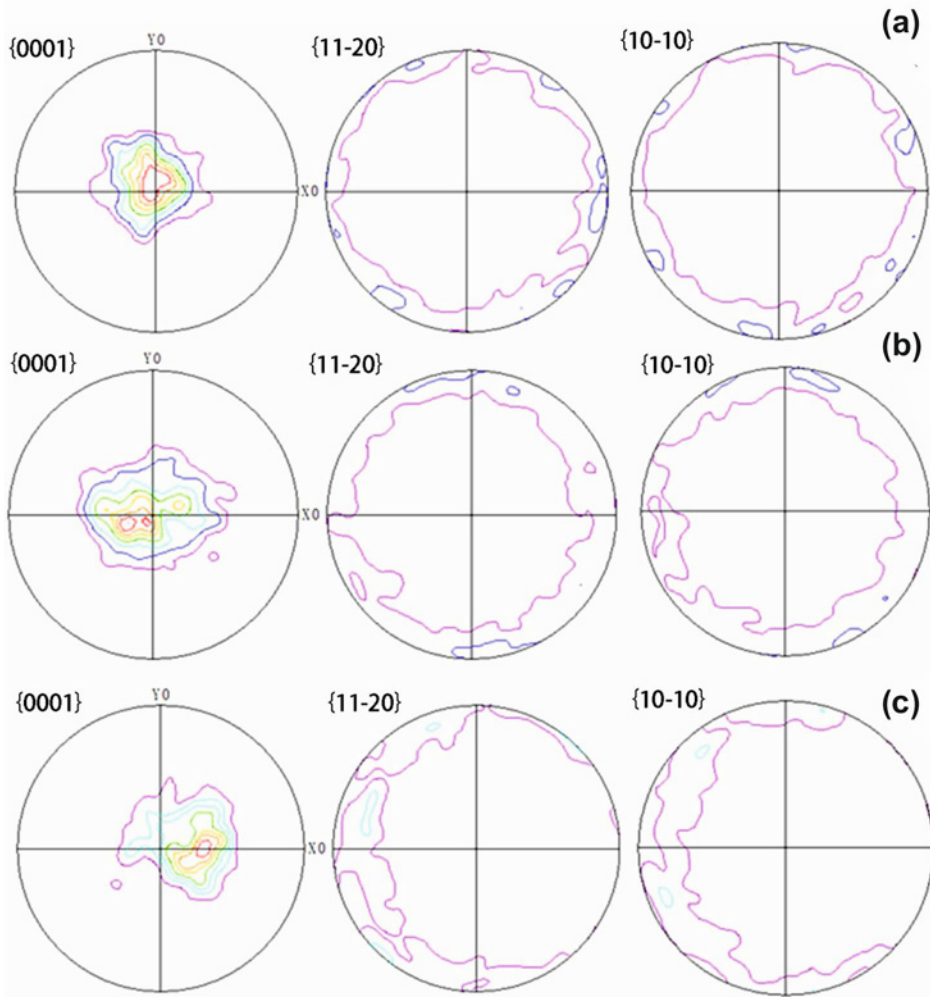


Fig. 8. Pole figures of specimens deformed at (a) 523 K & 0.001 s^{-1} , (b) 573 K & 0.001 s^{-1} , (c) 623 K & 0.001 s^{-1} , and (d) 673 K & 0.001 s^{-1} .

nents of the basal slip are divergent and obvious. The pole density of {0001} basal surface in the ND direction of plate is 11.55, and the {10̄10} cylinder does not form obvious preferred orientation, and the orientation of cylinder is more uniform around the polar circle. With the temperature increases, the texture deflects in a certain direction, and the angle between the deflection direction and RD direction is about 30° (Fig. 8b). The deflection of grain direction changes the density of textures, and it indicates that after the compression deformation of alloys in the flange holder region, a part of grains rotates in the direction of 30° to RD, which decreases the textures of the basal plane (Fig. 8c).

4. Conclusions

In the present work, the isothermal hot compression deformation was used to investigate the flow stress, processing characteristics and DRX behavior

of Mg-Zn-Zr alloys. The main conclusions are summarized as follows:

1. The studied Mg alloy exhibits an obvious flow softening behavior at compression deformation temperature of 523–673 K and strain rates of $0.001\text{--}1\text{ s}^{-1}$. Based on the strain-stress curves of Mg-Zn-Zr alloys, the flow stress decreases with increasing of deformation temperature or decreasing of strain rates.

2. Depending on the microstructure observation and calculated processing maps, the optimum hot-working condition for this Mg alloys is determined to be in temperature range of 593–623 K and strain rates of $0.01\text{--}0.001\text{ s}^{-1}$ with the peak value of PDE which is to reach 37 %. It is observed that the Medium Gaussian Kernel ($R = 0.9806$, AARE = 3.28 %) has better predicting capacity.

3. With temperature increasing, the sub-structures walled by LAGBs gradually decrease, while a corresponding increment on the recrystallized grains as the number of HAGBs increases. Meanwhile, the deflection of grain direction changes the density of textures,

and it indicates that after the compression deformation of alloys in the flange holder region, a part of grains rotates in the direction of 30° to RD, which decreases the textures of basal plane.

Acknowledgements

This work was supported by the College Students' Innovative Entrepreneurial Training Plan Program of Liaoning Province (Grant No. S202210148033), and Research Initiation Funds for Liaoning Petrochemical University (Grant No. 2019XJJ-001).

References

- [1] W. Liao, B. Ye, L. Zhang, H. Zhou, W. Guo, Q. Wang, W. Li, Microstructure evolution and mechanical properties of SiC nanoparticles reinforced magnesium matrix composite processed by cyclic closed-die forging, *Mater. Sci. Eng. A* 642 (2015) 49–56. <https://doi.org/10.1016/j.msea.2015.06.079>
- [2] Y. X. Liu, M. Curioni, Z. Liu, Correlation between electrochemical impedance measurements and corrosion rates of Mg-1Ca alloy in simulated body fluid, *Electrochim. Acta* 264 (2018) 101–108. <https://doi.org/10.1016/j.electacta.2018.01.121>
- [3] X. B. Zhang, G. Y. Yuan, L. Mao, J. L. Niu, P. H. Fu, W. J. Ding, Effects of extrusion and heat treatment on the mechanical properties and biocorrosion behaviors of a Mg-Nd-Zn-Zr alloy, *J. Mech. Behav. Biomed. Mater.* 7 (2012) 77–86. <https://doi.org/10.1016/j.jmbbm.2011.05.026>
- [4] E. K. Brooks, S. Der, M. T. Ehrensberger, Corrosion and mechanical performance of AZ91 exposed to simulated inflammatory conditions, *Mater. Sci. Eng. C* 60 (2016) 427–436. <https://doi.org/10.1016/j.msec.2015.11.059>
- [5] M. Hamed, Constitutive behaviors of magnesium and Mg-Zn-Zr alloy during hot deformation, *Mater. Chem. Phys.* 152 (2015) 123–126. <https://doi.org/10.1016/j.matchemphys.2014.12.023>
- [6] S. W. Xu, S. Kamado, N. Matsumoto, T. Honma, Y. Kojima, Recrystallization mechanism of as-cast AZ91 magnesium alloy during hot compressive deformation, *Mater. Sci. Eng. A* 527 (2009) 52–60. <https://doi.org/10.1016/j.msea.2009.08.062>
- [7] A. Bussiba, A. B. Artzy, A. Shtechman, S. Iferman, M. Kupiec, Grain refinement of AZ31 and ZK60 Mg alloys-towards superplasticity studies, *Mater. Sci. Eng. A* 302 (2001) 56–62. [https://doi.org/10.1016/S0921-5093\(00\)01354-X](https://doi.org/10.1016/S0921-5093(00)01354-X)
- [8] J. H. Li, Y. B. Zhang, Y. F. Wang, Q. Zeng, Y. Zhuang, Investigation on microstructure, mechanical properties and work hardening behavior of as-extruded Mg-4.5Zn-0.75Y-xZr alloys, *Mater. Res. Express.* 6 (2019) 126558. <https://doi.org/10.1088/2053-1591/ab57c1>
- [9] X. Xia, Q. Chen, K. Zhang, Z. Zhao, M. Ma, Hot deformation behavior and processing map of coarse-grained Mg-Gd-Y-Nd-Zr alloy, *Mater. Sci. Eng. A* 587 (2013) 283–290. <https://doi.org/10.1016/j.msea.2013.08.066>
- [10] H. Takuda, H. Fujimoto, N. Hatta, Modelling on flow stress of Mg-Al-Zn alloys at elevated temperatures, *J. Mater. Process. Tech.* 80 (1998) 513–516. [https://doi.org/10.1016/S0924-0136\(98\)00154-X](https://doi.org/10.1016/S0924-0136(98)00154-X)
- [11] M. A. J. Taleghani, J. M. Torralba, Hot deformation behavior and workability characteristics of AZ91 magnesium alloy powder compacts – A study using processing map, *Mater. Sci. Eng. A* 580 (2013) 142–149. <https://doi.org/10.1016/j.msea.2013.04.071>
- [12] D. Liu, Y. Liu, Y. Zhao, Y. Huang, M. Chen, The hot deformation behavior and microstructure evolution of HA/Mg-3Zn-0.8Zr composites for biomedical application, *Mater. Sci. Eng. C* 77 (2017) 690–697. <https://doi.org/10.1016/j.msec.2017.03.239>
- [13] J. D. Robson, D. T. Henry, B. Davis, Particle effects on recrystallization in magnesium–manganese alloys: particle pinning, *Mater. Sci. Eng. A* 528 (2011) 4239–4247. <https://doi.org/10.1016/j.msea.2011.02.030>
- [14] S. S. Zhou, K. K. Deng, J. C. Li, K. B. Nie, F. J. Xu, H. F. Zhou, J. F. Fan, Hot deformation behavior and workability characteristics of bimodal size SiCp/AZ91 magnesium matrix composite with processing map, *Mater. Des.* 64 (2014) 177–184. <https://doi.org/10.1016/j.matdes.2014.07.039>
- [15] H. Zhou, Q. D. Wang, B. Ye, W. Guo, Hot deformation and processing maps of as-extruded Mg-9.8Gd-2.7Y-0.4Zr Mg alloy, *Mater. Sci. Eng. A* 576 (2013) 101–107. <https://doi.org/10.1016/j.msea.2013.03.090>
- [16] C. S. Goh, J. Wei, L. C. Lee, M. Gupta, Properties and deformation behaviour of Mg-Y₂O₃ nanocomposites, *Acta Mater.* 55 (2007) 5115–5121. <https://doi.org/10.1016/j.actamat.2007.05.032>
- [17] R. Gehrmann, M. M. Frommert, G. Gottsteins, Texture effects on plastic deformation of magnesium, *Mater. Sci. Eng. A* 395 (2005) 338–349. <https://doi.org/10.1016/j.msea.2005.01.002>
- [18] J. Koike, T. Kobayashi, T. Mukai, H. Watanabe, M. Suzuki, K. Maruyama, K. Higashi, The activity of non-basal slip systems and dynamic recovery at room temperature in fine-grained AZ31B magnesium alloys, *Acta Mater.* 51 (2003) 2055–2065. [https://doi.org/10.1016/S1359-6454\(03\)00005-3](https://doi.org/10.1016/S1359-6454(03)00005-3)
- [19] A. Sadeghi, M. Pekguleryuz, Recrystallization and texture evolution of Mg-3%Al-1%Zn-(0.4-0.8)%Sr alloys during extrusion, *Mater. Sci. Eng. A* 528 (2011) 1678–1685. <https://doi.org/10.1016/j.msea.2010.10.096>
- [20] M. Golrang, M. Mobasher, H. Mirzadeh, M. Emamy, Effect of Zn addition on the microstructure and mechanical properties of Mg-0.5Ca-0.5RE magnesium alloy, *J. Alloys Compd.* 815 (2020) 152380. <https://doi.org/10.1016/j.jallcom.2019.152380>
- [21] Z. Z. Gui, Z. X. Kang, Y. Y. Li, Mechanical and corrosion properties of Mg-Gd-Zn-Zr-Mn biodegradable alloy by hot extrusion, *J. Alloys Compd.* 685 (2016) 222–230. <https://doi.org/10.1016/j.jallcom.2016.05.241>
- [22] M. Masoumi, F. Zarandi, M. Pekguleryuz, Microstructure and texture studies on twin-roll cast AZ31 (Mg-3wt.%Al-1wt.%Zn) alloy and the effect of thermomechanical processing, *Mater. Sci. Eng. A* 528 (2010) 1268–1279. <https://doi.org/10.1016/j.msea.2010.10.003>
- [23] S. A. Farzadfar, É. Martin, M. Sanjari, E. Es-

- sadiqi, M. A. Wells, S. Yues, On the deformation, recrystallization and texture of hot-rolled Mg-2.9Y and Mg-2.9Zn solid solution alloys – A comparative study, *Mater. Sci. Eng. A* 534 (2012) 209–219. <https://doi.org/10.1016/j.msea.2011.11.061>
- [24] E. Dogan, M. W. Vaughan, S. J. Wang, I. Karaman, G. Proust, Role of starting texture and deformation modes on low-temperature shear formability and shear localization of Mg-3Al-1Zn alloy, *Acta Mater.* 89 (2015) 408–422. <https://doi.org/10.1016/j.actamat.2014.12.006>
- [25] A. A. Roostaei, A. Zarei-Hanzaki, H. R. Abedi, M. R. Roknis, An investigation into the mechanical behavior and microstructural evolution of the accumulative roll bonded AZ31 Mg alloy upon annealing, *Mater. Des.* 32 (2011) 2963–2968. <https://doi.org/10.1016/j.matdes.2011.01.038>
- [26] B. Zhang, Y. Wang, L. Geng, C. Lus, Effects of calcium on texture and mechanical properties of hot-extruded Mg-Zn-Ca alloys, *Mater. Sci. Eng. A* 539 (2012) 56–60. <https://doi.org/10.1016/j.msea.2012.01.030>